J. Fluid Mech. (2000), *vol.* 407, *pp.* 265–290. Printed in the United Kingdom

The role of dissipation and mixing in exchange flow through a contracting channel

By KRAIG B. WINTERS[1]† AND HARVEY E. SEIM[2]

[1] Applied Physics Laboratory and Department of Applied Mathematics, University of Washington, Seattle, WA, USA

[2]Skidaway Institute of Oceanography, 110 Ocean Circle, Savannah, GA 31411, USA

(Received 26 August 1998 and in revised form 17 May 1999)

We investigate the transport of mass and momentum between layers in idealized exchange flow through a contracting channel. Lock-exchange initial value problems are run to approximately steady state using a three-dimensional, non-hydrostatic numerical model. The numerical model resolves the large-scale exchange flow and shear instabilities that form at the interface, parameterizing the effects of subgrid-scale turbulence. The closure scheme is based on an assumed steady, local balance of turbulent production and dissipation in a density-stratified fluid.

The simulated flows are analysed using a two-layer decomposition and compared with predictions from two-layer hydraulic theory. Inter-layer transport leads to a systematic deviation of the simulated maximal exchange flows from predictions. Relative to predictions, the observed flows exhibit lower Froude numbers, larger transports and wider regions of subcritical flow in the contraction. To describe entrainment and mixing between layers, the computed solutions are decomposed into a three-layer structure, with two bounding layers separated by an interfacial layer of finite thickness and variable properties. Both bounding layers lose fluid to the interfacial layer which carries a significant fraction of the horizontal transport. Entrainment is greatest from the faster moving layer, occurring preferentially downstream of the contraction.

Bottom friction exerts a drag on the lower layer, fundamentally altering the overall dynamics of the exchange. An example where bed friction leads to a submaximal exchange is discussed. The external forcing required to sustain a net transport is significantly less than predicted in the absence of bottom stresses.

1. Introduction

Flow between two basins of different fluid densities is a long-standing problem of fundamental interest in geophysical fluid dynamics. Such flows occur frequently in nature, for example in straits, in channels between deep ocean basins, or between lagoons and coastal seas. Typically, these flows are driven by internal pressure gradients resulting from the density contrast between the basins and are strongly influenced by topographical features of connecting channels. Depending on the sign and the magnitude of the barotropic pressure difference between the basins, such flows can be either uni- or bi-directional. In the case of bi-directional or exchange flow, the net (vertically averaged) flow can be in either direction.

Scientific interest in the dynamics of exchange flows dates from at least as early as

† Also at the Centre for Water Research, University of Western Australia, Nedlands, WA, Australia.

1681 when Marsigli performed his experiments to explain the counter-flow through the Bosphorus. In the Bosphorus, salinity differences between the Mediterranean Sea to the south, and the Black Sea to the north, drive an under-current northward through the strait, while a difference in sea level drives a south-flowing surface current. Generally, the net transport is from north to south. The strait itself has a distinct contraction which appears to be a site of persistent and energetic mixing of the opposing flows (Oğuz *et al.* 1990).

Theoretical understanding of exchange flows is based largely on equations describing the dynamics of steady, inviscid two-layer flows through idealized channels with slowly varying cross-sectional area. Analytical treatments for two-layer flow through a contracting channel are given by Armi & Farmer (1986) and Lawrence (1990). Two-layer hydraulic theory predicts the height of the interface separating the layers and the streamwise dependence of the layer speeds, given the channel geometry, the densities of the layers and the net transport (or the flow rate ratio).

Arguably the most important concept emerging from these analyses is that of maximal exchange. When two hydraulic controls are present, the volumetric exchange between two basins is determined by processes occurring within the region defined by the controls, this region being isolated from the basins by two distinct zones of supercritical flow. This exchange is maximal in the sense that no greater exchange can occur (Armi & Farmer 1987), i.e. no solutions of the idealized hydraulic equations with greater exchange exist.

Though two-layer hydraulic theory has proven extremely useful, direct application of the theory to geophysical flows of interest is often problematic. In particular, the theory excludes entrainment and mixing between layers and thus cannot be used to address the streamwise variability of the active and passive tracers in the opposing flows. The flow through the Strait of Gibraltar provides a good example. Bray, Ochoa & Kinder (1995) observed a thick interfacial layer with variable properties in Gibraltar, concluding that this layer was the result of vertical exchange and mixing between the upper and lower layer flows. Furthermore, the interfacial layer was observed to carry a significant fraction of the horizontal transport in both directions. Though the hydraulic theory can be extended to three or more layers of uniform properties (see e.g. Baines 1995) the resulting framework does not allow for the transport of properties between layers.

In this paper we take a numerical approach and examine simulations of exchange flow through idealized contracting channels. In taking this approach, several of the simplifying assumptions of two-layer hydraulic theory are relaxed. Numerical solutions are obtained for non-hydrostatic flow of a continuously stratified fluid in three dimensions. The numerical results are first examined within the framework of the two-layer theory; however our particular focus is on the effects and consequences of mixing and dissipation. The numerical study is by no means exhaustive; only a few representative simulations covering a limited portion of the relevent parameter space are discussed.

We show that an interfacial layer of intermediate density plays an important role in the horizontal exchange. This layer is formed by vertical entrainment and mixing in the vicinity of the controls, and carries mixed fluid away from the contraction in both directions. The transport in the interfacial layer is significant; it can equal or exceed the transport of unmixed fluid. These findings are similar to those of Bray *et al.* (1995) for Gibraltar. We also give an example where the effect of bottom stress is to inhibit the development of supercritical flow in the lower layer, resulting in a submaximal exchange flow.

We begin by slightly re-casting the 'canonical' problem of two-layer exchange flow to facilitate a numerical approach (§ 2) followed by a brief description of the numerical methods used to simulate the flow (§ 3). In § 4, simulations of maximal exchange flow through a free-slip channel are analysed. The results are interpreted from both a two- and three-layer perspective and the exchange between layers is quantified. In § 5, we discuss a simulation of submaximal exchange in which bottom friction acts to slow the lower layer flow. These results are also interpreted from two- and three-layer perspectives. A discussion of the results is given in § 6.

2. Exchange flows: IVP formulation

Steady two-layer hydraulic theory for flow through a contraction is based on continuity and the dimensionless Bernoulli equations for the upper (subscript 1) and lower (subscript 2) layers,

$$Q = b(u_1 h_1 + u_2 h_2), \tag{1}$$

$$H_1 = \tfrac{1}{2}u_1^2(x) + \frac{g}{g'} + P_s(x), \tag{2}$$

$$H_2 = \tfrac{1}{2}u_2^2(x) + \frac{\rho_1}{\Delta\rho}h_1 + \frac{g}{g'}h_2 + P_s(x) \tag{3}$$

focusing on the energy difference $\Delta H = H_2 - H_1$ to emphasize the internal dynamics. Here Q is the net transport, $b(x)$ is the channel width, $\Delta\rho = \rho_2 - \rho_1$, $g' = g\Delta\rho/\rho_2$ is the reduced gravity, and P_s is the surface pressure assuming a stress-free rigid lid. Layer thicknesses h_i and velocities u_i are scaled by the (uniform) channel depth D and the nominal wave speed $\sqrt{g'D}$ respectively.

Hydraulic control occurs at locations where the composite Froude number G^2 is equal to one (Armi & Farmer (1986)), where

$$G^2 = F_1^2 + F_2^2, \quad F_i^2 = \frac{u_i^2}{h_i}. \tag{4}$$

Two-layer flow is subcritical when $G^2 < 1$ and supercritical for $G^2 > 1$. Maximal exchange flow through contracting channels is characterized by the existence of two control points: a throat control at the narrowest section and a virtual control located upstream (with respect to the net transport) of the throat. For exchange flow with no directional bias, these two control points coalesce at the throat.

To predict maximal exchange solutions using two-layer hydraulic theory, the channel width $b(x)$, the depth D, the density difference $\Delta\rho$ and either the net transport Q or the ratio of the layer transports q_r, where

$$q_r = \frac{q_1}{|q_2|} \tag{5}$$

are specified. Determination of the conditions at the throat and virtual controls is sufficient to determine steady solutions for the volumetric transport, the thickness and the velocity of the layers (Armi & Farmer 1986; Lawrence 1990). For submaximal exchange, the virtual control is not present and flow conditions at another point, e.g. at the subcritical channel exit, must be used instead to close the problem. Note that in either case, either the net transport or the transport ratio must be specified to determine the solution.

Figure 1 shows the plan view of the contracting channel used for the numerical simulations as well as the two-layer hydraulic prediction of G^2 for the density

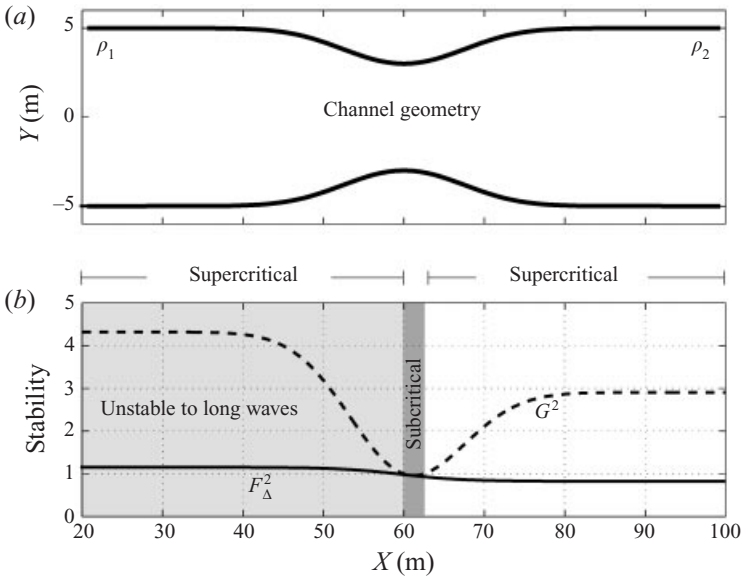

FIGURE 1. (*a*) Plan view of the contracting channel used in the numerical simulations. Basins to the left (right) of the channel are sources of fluid with density ρ_1 (ρ_2). (*b*) Composite (G^2) and stability (F_Δ)^2 Froude numbers.

difference used in the simulations. In this example, the transport ratio q_r is less than one and the net transport is from right to left. Dark shading marks the region of predicted subcritical flow where $G^2 < 1$. To either side of this region, the flow is supercritical. Though not explicitly predicted by the theory, it is understood that supercritical conditions will not be maintained and that the flow will return to a subcritical state via dissipative hydraulic jumps. Also shown in the figure is the stability Froude number $F_\Delta = (u_2 - u_1)/\sqrt{g'D}$, a measure of the long-wave stability (Lawrence 1990). Note that most of the flow downstream of the contraction (light shading) is predicted to be unstable to long waves. Since two-layer hydraulic theory is based on the propagation of information via long internal waves, the theory is self-inconsistent in this region.

Suppose we wish to view these steady hydraulic predictions as far-field (in time) solutions of lock-exchange, initial-value problems in a variable-width channel. At $t = 0$, we know, and can thus specify, the channel geometry and the densities of the two fluids in the adjoining reservoirs. We do not know however, and thus cannot specify, the flow rate ratio or the net (vertically averaged) flow. This is part of the solution of a well-posed initial-boundary value problem. Intuitively, the pressure difference across the contraction would appear sufficient to complete the problem specification. Note that specifying Q or q_r allows the hydraulics solution to be obtained (Armi & Farmer 1986; Lawrence 1990). In particular, the solution yields the upper-layer velocity $u_1(x)$ which, via (2), determines the surface pressure $P_s(x)$ up to a constant. In this way, a unique relationship between the pressure drop across the contraction ΔP and either Q or q_r can be computed for a given channel geometry and density difference.

The ΔP vs. q_r relationship allows the problem statement for steady exchange flow through a variable-width channel to be re-cast slightly. The external parameters are the channel geometry ($b(x)$ and H), the density difference between the reservoirs $\Delta\rho$

and the pressure drop across the contraction ΔP. This formulation is convenient for numerical simulation and also facilitates comparison of results with two-layer hydraulic predictions. Assuming infinite reservoirs, this approach also allows the problem to be formulated within a section of the channel encompassing the control points but not necessarily including the reservoirs themselves. This has the advantage of focusing computational effort in the vicinity of the hydraulic controls and their associated jumps. Reservoir conditions enter the problem formulation only indirectly via the specification of the inflow densities (or tracer concentrations). The layer thicknesses, i.e. the locations of in- and outflow at the up- and downstream computational boundaries, are not specified *a priori* but change in time and are determined as part of the solution.

The computational approach taken here is to begin with 'lock-exchange' initial conditions in a finite length channel. Steady solutions to the full equations of motion are then computed and compared to the corresponding theoretical predictions. For the simulations discussed, the primary external variable to be varied is the barotropic pressure drop across the contraction, with the channel geometry and the density difference held fixed.

3. Numerical model

The equations of motion for an incompressible, density stratified fluid under the Boussinesq approximation are

$$\frac{\partial}{\partial t}\boldsymbol{u} + \boldsymbol{u}\cdot\nabla\boldsymbol{u} = -\frac{1}{\rho_0}\nabla p - \hat{\boldsymbol{z}}\frac{g}{\rho_0}\rho' + \nabla\cdot K_m\nabla\boldsymbol{u}, \tag{6}$$

$$\frac{\partial}{\partial t}\rho' + \boldsymbol{u}\cdot\nabla\rho' + w\frac{\mathrm{d}}{\mathrm{d}z}\bar{\rho} = \nabla\cdot K_T\nabla\rho', \tag{7}$$

$$\nabla\cdot\boldsymbol{u} = 0. \tag{8}$$

Here $\boldsymbol{u}$ is the velocity vector with components $[u, v, w]$ in the cartesian coordinate directions x, y and z, ρ' is the density perturbation from an arbitrarily specified, time independent profile $\bar{\rho}(z)$, ρ_0 is a constant reference density, g is the gravitational acceleration and $\hat{\boldsymbol{z}}$ is the unit vector in the vertical direction (positive upward). The coefficients K_m and K_T are the eddy viscosity and eddy diffusivity respectively, with values that vary in space and time depending on local estimates of the production rate of turbulent kinetic energy.

Equations (6)–(8) are solved numerically over an orthogonal-curvilinear grid conforming to the variable width channel sidewalls. All simulations discussed in this paper were conducted for the 120 m long by 10 m deep channel shown in figure 1. The resolution of the numerical mesh was $129 \times 17 \times 65$ grid points in the streamwise x, spanwise y and vertical z directions respectively. Though the horizontal spacings are variable in curvilinear coordinates, this corresponds to nominal grid spacings of 93, 60 and 15 cm.

The numerical algorithm incorporates a fourth-order compact scheme for spatial differentiation, third-order Adams–Bashforth time stepping and a multi-grid projection method for pressure. A discussion of the numerical methods, as well as a suite of validation studies against analytical solutions and a laboratory experiment, are given in Winters, Seim & Finnigan (2000). Two aspects of the numerical methods, however, are specific to these exchange flow simulations and warrant further discussion. The subgrid-scale closure scheme, by which the values of the eddy viscosity and diffusivity

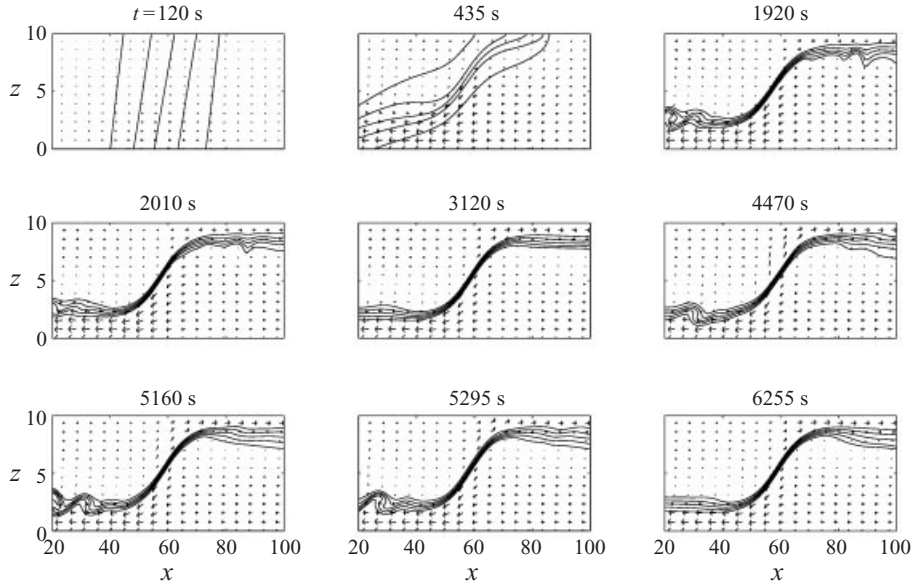

FIGURE 2. Snapshots of the velocity vectors, overlain with contours of the density field, for various times during the evolution of the initial value problem to steady state. For this case $q_r = 0.55$. Simulation data are taken from the mid-channel, vertical (x, z)-plane.

are prescribed and the treatment of the open boundary conditions are presented in the Appendix.

The simulations are conducted in a variable-width channel with vertical, free-slip sidewalls. The free surface is treated as a stress-free rigid lid, consistent with the Boussinesq approximation (see Lawrence 1990). The maximal exchange simulations in § 4 were computed with a free-slip bottom boundary. For the submaximal flow in § 5, the effects of bottom stress were included and a no-slip bottom boundary condition was imposed. At all solid walls, adiabatic zero-flux conditions are prescribed for density. At the up- and downstream computational boundaries, the inflow densities are prescribed to match the assumed reservoir values. Viscous sponge layers are employed within 20 m of these open boundaries to minimize spurious reflections from imperfect treatment of the open boundaries.

4. Maximal exchange flow

4.1. *Overview*

The simulations are initialized as lock-exchange problems: fluids of slightly different density ($\Delta\rho = 0.5\,\mathrm{kg\,m^{-3}}$) fill the two ends of the channel, separated by a gradual transition region centred at the channel narrows. A barotropic pressure drop, with higher pressure at the left end of the channel, is prescribed via the boundary conditions and maintained as the flow develops. Figure 2 shows the formation of bore-like features near the top and bottom of the channel which propagate away from the contraction and out of the channel. The isopycnal positions in the vicinity of the contraction are established quickly, indicating relatively rapid establishment of hydraulic control, which is maintained as the flow continues to accelerate. Non-hydrostatic features, associated with the bore fronts and their instabilities, propagate out of the test section, into the sponge regions and out of the computational domain, leaving behind an

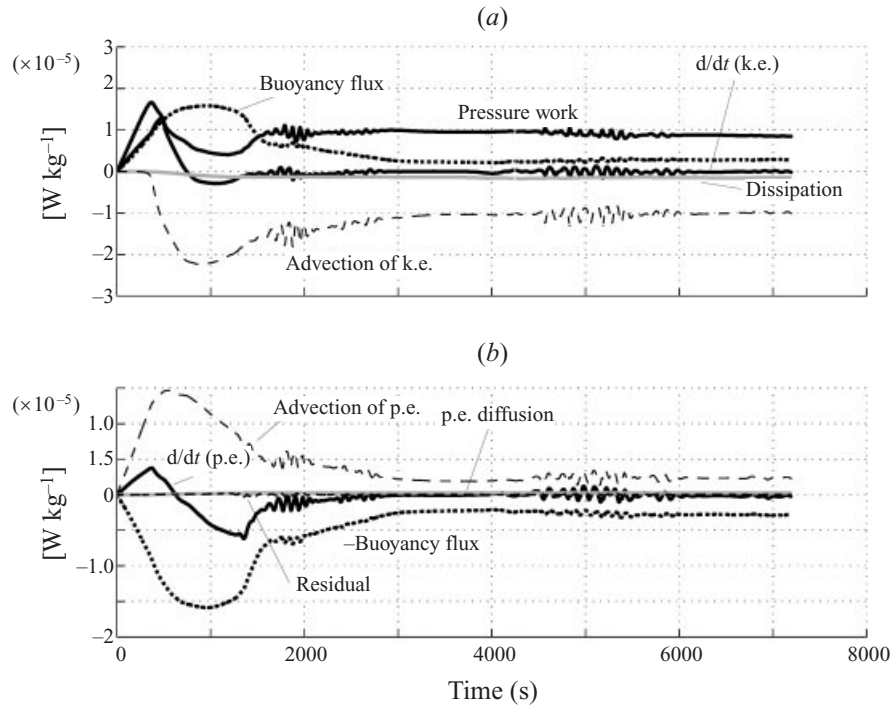

FIGURE 3. Components of (*a*) the kinetic energy balance and (*b*) potential energy balance for the simulation shown in figure 2.

approximately steady exchange flow with no indication of significant reflection from the artificial boundaries.

Energy balance equations for the computational domain V can be derived from the equations of motion (6)–(8) (Winters *et al.* 1995). Kinetic (E_k) and potential energy (E_p) obey the evolution equations

$$\frac{\mathrm{d}}{\mathrm{d}t}E_k = \frac{-1}{\rho_0 V}\oint_S \left[p\boldsymbol{u} + \boldsymbol{u}\frac{(u^2+v^2+w^2)}{2}\right]\cdot\hat{\boldsymbol{n}}\,\mathrm{d}S - \frac{g}{\rho_0 V}\int_V \rho w\,\mathrm{d}V + \frac{1}{\rho_0 V}\int_V \boldsymbol{u}\cdot\nabla\cdot K_m\nabla\boldsymbol{u}\,\mathrm{d}V, \tag{9}$$

$$\frac{\mathrm{d}}{\mathrm{d}t}E_p = \frac{g}{\rho_0 V}\int_V \rho w\,\mathrm{d}V + \frac{g}{\rho_0 V}\oint_S z\rho\boldsymbol{u}\cdot\hat{\boldsymbol{n}}\,\mathrm{d}S + \frac{g}{\rho_0 V}\int_V z\nabla\cdot K_T\nabla\rho\,\mathrm{d}V, \tag{10}$$

where

$$E_p = \frac{g}{\rho_0 V}\int \rho z\,\mathrm{d}V, \quad E_k = \frac{1}{\rho_0 V}\int \frac{u^2+v^2+w^2}{2}\mathrm{d}V \tag{11}$$

and S is the surface bounding the computational domain V with outward facing unit normal $\hat{\boldsymbol{n}}$.

The time-dependent energy balances in figure 3 demonstrate the approach of the lock-exchange problem to a nearly steady exchange flow for which the various energy transfer terms remain approximately constant. Early in the development, i.e. over the first 3000 s, the bore-like signals propagate toward the boundaries and out of the system. During this time, instabilities are observed near the bore fronts

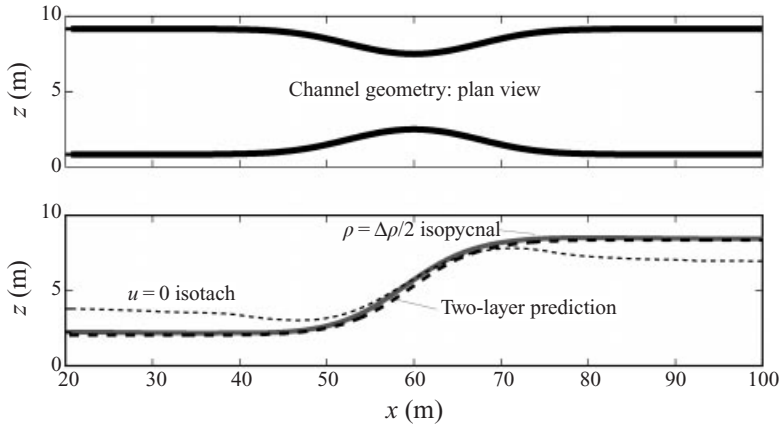

FIGURE 4. A comparison of the predicted and simulated interface heights as a function of streamwise position for $q_r = 0.59$, typical of all the maximal exchange simulations. A feature suggestive of a weak hydraulic jump is apparent in the simulated velocity interface but not in the density interface.

and the resulting energy balances are strongly time dependent. After about 3000 s, only occasional bursts of instabilities near the contraction exit (the left exit in this example) are observed. These instabilities lead to wave-like fluctuations in the time rate of change terms. On the whole, however, a steady balance is maintained.

The kinetic energy equation is well approximated by a three-term balance between pressure work, buoyancy flux and loss of kinetic energy by advection out of the domain. The potential energy equation reduces to an approximate balance between potential energy advection and buoyancy flux. These balances describe a system in which, on average, heavy fluid parcels are advected into the domain slowly and at height to the right, which then gain kinetic and lose potential energy as they accelerate and plunge through the contraction, before exiting the domain at higher velocity and lower elevation to the left. The residual of the potential energy balance is always small relative to the dominant forcing terms of the problem, typically less than 1% of the kinetic energy advection or the pressure work terms. Because the energy balance is assessed independently of the calculations used to advance the fields in time, the magnitude of the potential energy balance residual is a good indicator of the overall quality of the numerical solution.

4.2. *Two-layer decomposition*

To permit a comparison between the model results and inviscid theory we time- and cross-channel average the simulated fields once an approximately steady state (as indicated by the energy transfer terms) had been established. For the purpose of forming layer Froude numbers, the zero isotach of the averaged flow is used to decompose the flow into two layers. The lower-layer thickness h_2 is taken as the height of the zero-crossing of the averaged streamwise flow and the upper layer h_1 is equal to $H - h_2$. Layer velocities u_i are computed by averaging u within each layer. Layer transports $q_i = u_i h_i b$ are then computed as a function of streamwise position and the average value of $q_1/|q_2|$ is taken to characterize the flow for comparison with analytical predictions.

Alternatively, the mid-isopycnal $\Delta\rho/2$ could be used to separate the flow. Note that these two surfaces are not co-located in the domain (figure 4). We use the zero isotach to define the layers because this definition seems more consistent with the spirit of

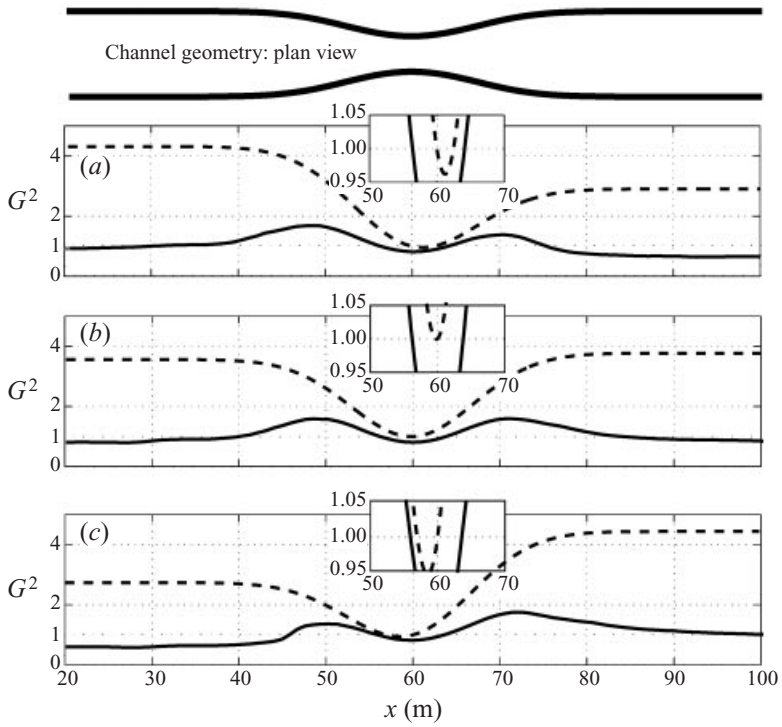

FIGURE 5. Comparison of predicted (dashed line) and simulated (solid line) streamwise distributions of the composite Froude number G^2 for (*a*) $q_r = 0.59$, (*b*) $q_r = 1.02$ and (*c*) $q_r = 1.92$. A blow-up of the graphic near the throat of the contraction is shown as an insert.

the theory, i.e. two layers of fluid flowing in opposite directions. Though our choice is somewhat arbitrary, we note that computation of Froude numbers based on layers defined by the position of the mid-isopycnal leads to results that are inconsistent with the observed character of the flow. For example, the lower-layer flow shown in figure 6 is laminar and free of instabilities as it nears the left exit of the domain. The lower layer Froude numbers, based on layers defined by the zero isotach and the mid-isopycnal, are approximately 0.44 and 2.7 respectively. Characterizing the lower-layer flow as highly supercritical does not seem reasonable. Similar inconsistencies were observed in all the maximal exchange simulations when the mid-isopycnal was used to define the two layers.

Figure 4 shows that the zero isotach is systematically offset from the predicted interface position. This is characteristic of all the model solutions with free-slip boundary conditions; the layers never get as thin as predicted by inviscid theory. Instead, there are adjustments to the height of the velocity interface downstream edges of the contraction (near 50 and 70 m), resulting in thicker than predicted active layers outside of the contraction. The separation of the density and velocity interfaces indicates that mixed fluid has been formed, and that it is moving away from the contraction on either side.

Predicted and simulated composite Froude numbers G^2 are shown in figure 5 for three different values of the flow rate ratio q_r. A number of features are common to all cases. Most apparent is that the predicted and simulated solutions agree best within the contraction region. Away from the contraction the simulated flows are subcritical

Q_r	ΔP_s	ΔP_p	$\frac{q_{1s}}{q_{1p}}$	$\frac{q_{2s}}{q_{2p}}$	$\frac{Q_s}{Q_p}$	$\frac{\Delta q_1}{q_{10}}$
0.59	−12.2	−10.9	1.13	1.13	1.13	−0.05(−0.08)*
1.02	−16.0	−15.7	1.09	1.09	1.09	0.00
1.92	−18.6	−21.1	1.14	1.14	1.14	0.03
1.73#	−9.4	−17.1	1.14	1.28	1.00	0.14

TABLE 1. Comparison of two-layer values from simulations (subscript s) and predictions (subscript p). (* indicates entrainment during a wave packet event; # indicates prediction is for submaximal flow where the observed Q was used to specify the problem, hence the predicted q_r (1.94) is not matched). q_{10} is the transport carried by the upper layer as it enters the computational domain. Pressures given in Pa.

whereas the theoretical predictions remain supercritical. Because the theory does not explicitly predict the location or the energy loss of jumps, this results in the large observed discrepancy in G^2. Within the contraction, the model results are similar to the predictions in that a subcritical region is observed, bounded to either side by zones of supercritical flow. This is the defining characteristic of maximal exchange flow (Armi & Farmer 1987). As predicted, maximum values of G^2 occur downstream of the contraction. When $q_r \approx 1$, the maxima on either side of the contraction are approximately equal. The exact positions of the controls (where $G^2 = 1$) are not accurately predicted by the theory; generally the subcritical region is significantly wider than predicted. The virtual control, which occurs upstream of the throat in the biased flows, is further upstream than predicted, while the throat control is shifted downstream. In these maximal exchange simulations, the throat of the contraction is therefore not a control point. In the case where $q_r = 1$, the theory predicts the coalescence of the virtual and the throat controls. In the simulations, however, the two controls remain separated.

Though mixing and dissipation at the interface does not qualitatively alter the nature of the simulated maximal exchange flows, it does lead to quantitative differences relative to inviscid predictions. The predicted and modelled pressure drop across the channel is roughly the same for $q_r = 1$, which we will denote as $\Delta P_{q_r=1.02}$. To drive a net rightward (leftward) transport through the channel, a larger (smaller) pressure drop is required. We find that the change in ΔP needed to shift the simulation from a pure exchange flow to one with a net transport is significantly less than that predicted from two-layer theory. In particular, the observed $\Delta P_{q_r=0.59} - \Delta P_{q_r=1.02} = 3.8$ whereas the predicted change is 4.8. Similarly, $\Delta P_{q_r=1.92} - \Delta P_{q_r=1.02} = 2.6$ while the predicted change is 5.4. This suggests that the change in external forcing needed to move the flow away from a pure exchange flow is reduced by as much as 50% when the flow is continuously stratified and subject to mixing and dissipation. At the same time the volume transport in the layers is moderately increased, presumably due to the shift in the control locations and the correspondingly greater active layer thickness.

The change in transport carried by the upper layer, Δq_1, reveals that fluid is systematically lost or gained by the upper layer depending on the value of q_r. When $q_r \approx 1$, the layer transport changes little. When $q_r < 1$ less fluid leaves the domain in layer 1 than enters it, i.e. layer 2 preferentially entrains fluid from layer 1. The reverse is true when $q_r > 1$; layer 1 entrains fluid from layer 2. When the flow is steady and free of shear instabilities roughly 5% of the flow is entrained when $q_r \neq 1$. When the interface is unstable (e.g. near $t = 5000$ in figures 2 and 3) the entrainment rate can double (table 1).

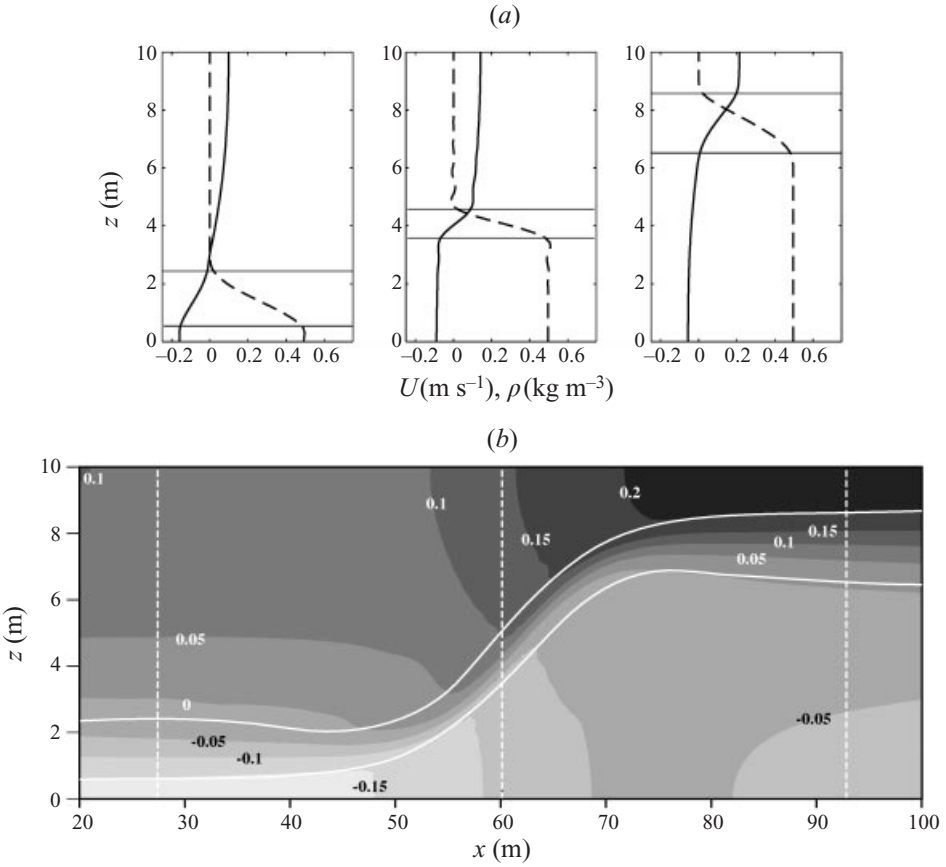

FIGURE 6. (*a*) Profiles of U (———) and ρ (– – –) from the three streamwise positions marked with dashed white lines on the contour plot (*b*). Horizontal lines mark the positions of the upper and lower bounds of the interfacial layer. (*b*) Contours of U (in $\mathrm{m\,s^{-1}}$) overlain with the upper and lower boundaries of the interfacial layer for $q_r = 1.92$.

4.3. *Three-layer decomposition*

A more careful examination of the continuous fields suggests a qualitative change in character of the flow as a result of entrainment and mixing between layers. The velocity and density profiles shown in figure 6(*a*) suggest the flow might be more appropriately described by three layers, with two bounding layers of approximately uniform properties being separated by a finite-thickness interface. Marked on the panels are the upper and lower limits of the interface layer, defined as a $0.05\,\mathrm{kg\,m^{-3}}$ difference from the inflow densities. Overlaying these interfaces on contours of the along-channel velocity field (figure 6*b*) shows that the interface layer is thinnest in the contraction and thicker to either side. It is also apparent that the zero isotach is not centred in the interfacial layer; rather, the interface is moving with the lower layer to the left of the contraction and with the upper layer to the right.

The relative importance of each of the three layers in carrying the transport, and the rate of entrainment into the interface from the bounding layers, is summarized in figure 7 for three values of q_r. The size of the circles shows the relative speed of the layer at various streamwise positions, filled circles denoting flow to the right, open circles flow to the left. Shading in the bounding layer indicates the rate of detrainment

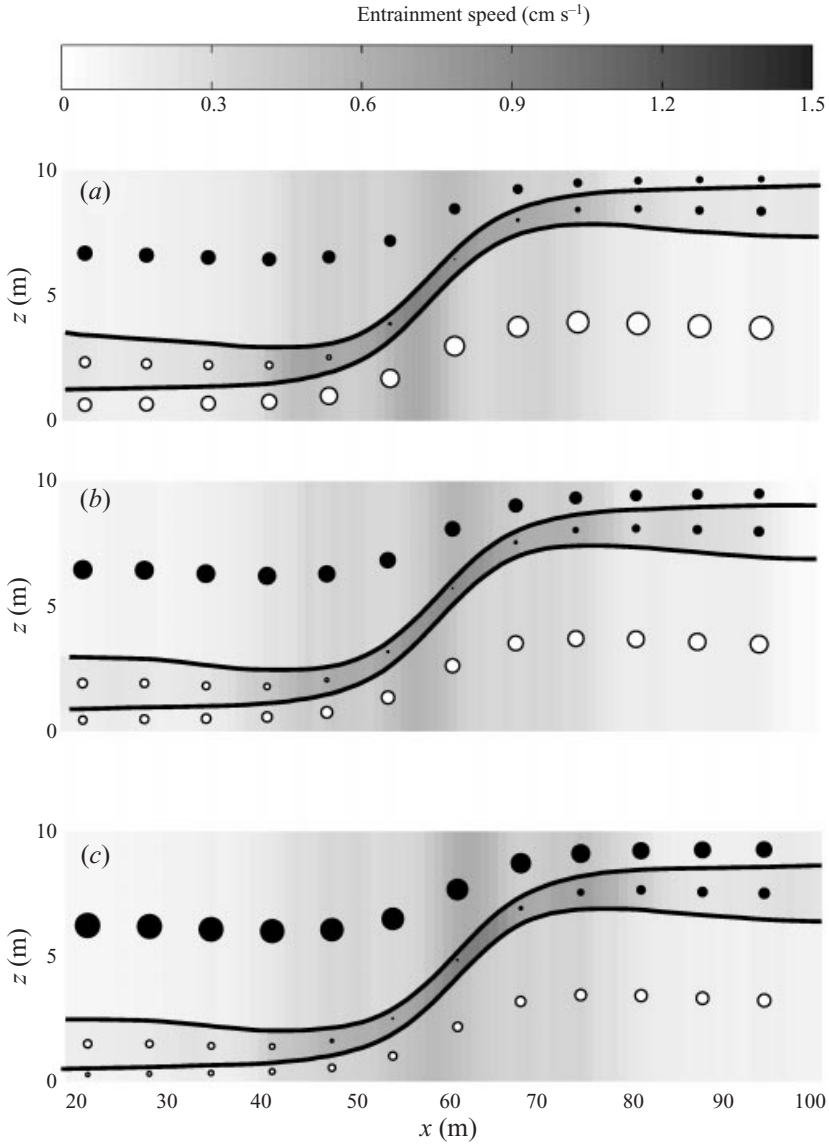

FIGURE 7. Three-layer representation of flows with (*a*) $q_r = 0.59$ (*b*) $q_r = 1.02$ and (*c*) $q_r = 1.92$. Thick lines show the positions of the upper and lower boundaries of the interfacial layer. Circles represent the magnitude of the streamwise transport in each layer, larger symbols indicating greater transport, with filled symbols denoting flow to the right, open symbols denoting flow to the left. Shading in the bounding layers indicates the detrainment speed (i.e. loss of fluid from the layer), and shading in the interfacial layer indicates the rate of entrainment from both bounding layers.

(i.e. rate of loss of transport) from the layers, and shading in the interfacial layer indicates the total entrainment from both bounding layers. Loss of transport from the bounding layers is a signature of diapycnal mixing. When $q_r = 1$, the bounding layers carry the same transport and both are entrained into the interfacial layer at about the same rate. The upper-layer transport decreases from left to right, with maximum rates of detrainment occurring to the right (i.e. downstream) of the contraction. The

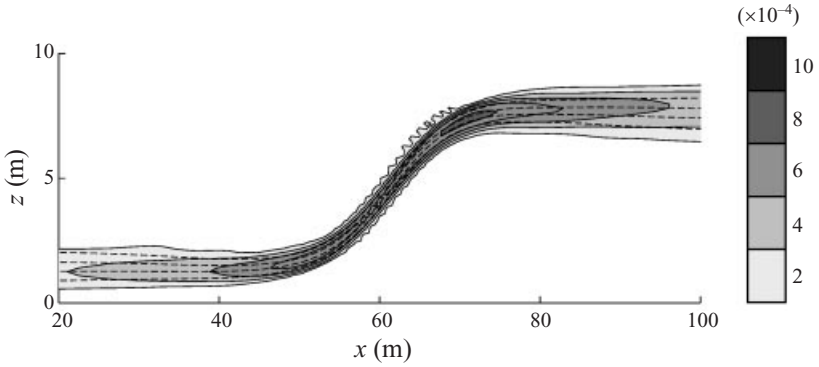

FIGURE 8. Contours of $K_m = K_T$ (in $\mathrm{m\,s^{-1}}$) for $q_r = 1.92$, overlain with isopycnals between 0.1 and $0.4\,\mathrm{kg\,m^{-3}}$. Note the symmetry of the distribution of K_m about the contraction, and the close correspondence in the positions of maximum K_m and the pycnocline.

lower-layer transport is the mirror image of that in the upper layer. The interfacial layer carries essentially no net transport at the centre of the contraction and roughly as much transport as the bounding layers near the channel exits. To either side of the contraction, local entrainment of fluid into the interfacial layer is preferentially from the faster of the two bounding layers. This is a consequence of the vertical asymmetry of the shear with respect to the location of the interfacial layer in the vicinity of the control points.

When $q_r \neq 1$, the flows are similar but the layer properties are no longer laterally symmetric across the throat of the contraction. The interfacial layer carries roughly the same transport as when $q_r \approx 1$, but because of the reduced transport in the slower moving bounding layer, the interfacial layer carries the majority of the transport in the upstream (with respect to the vertically averaged flow) direction. Entrainment remains concentrated in the region of the contraction and again occurs preferentially from the (locally) faster of the two layers.

Mixing rates are greatest where the density gradient and eddy diffusivity are large. The density conservation equation

$$\frac{\partial \rho}{\partial t} + \boldsymbol{u} \cdot \nabla \rho = \nabla \cdot K_T \nabla \rho \tag{12}$$

indicates that when the flow is steady, streamlines will cross isopycnals (i.e. there will be diapycnal transport) where the diffusivity K_T and density gradients are locally enhanced. Figure 8 shows elevated diffusivities within the interface layer, with peak values occurring to either side of the contraction. From figure 6(*b*) it can be seen that the sites of these maxima are also where the isotachs cross the isopycnals, i.e. where $\boldsymbol{u} \cdot \nabla \rho$ is non-zero. From the two-layer analysis, we see that (figure 5) these are also locations where the flow is supercritical or making a transition back to a subcritical state. These results are consistent with the notion that mixing is strongest where the flow speeds are highest or there are jumps.

The three-layer analysis emphasizes that the inclusion of viscosity and diffusion into the problem leads to a fundamental change in the character of the solution. Strong mixing in the exit regions of the contraction produces a significant amount of mixed fluid. The flow in the interface is typically away from the contraction. The composition of the interfacial layer is related to the relative speeds of the bounding layers, the faster moving layer being entrained more rapidly into the interfacial layer.

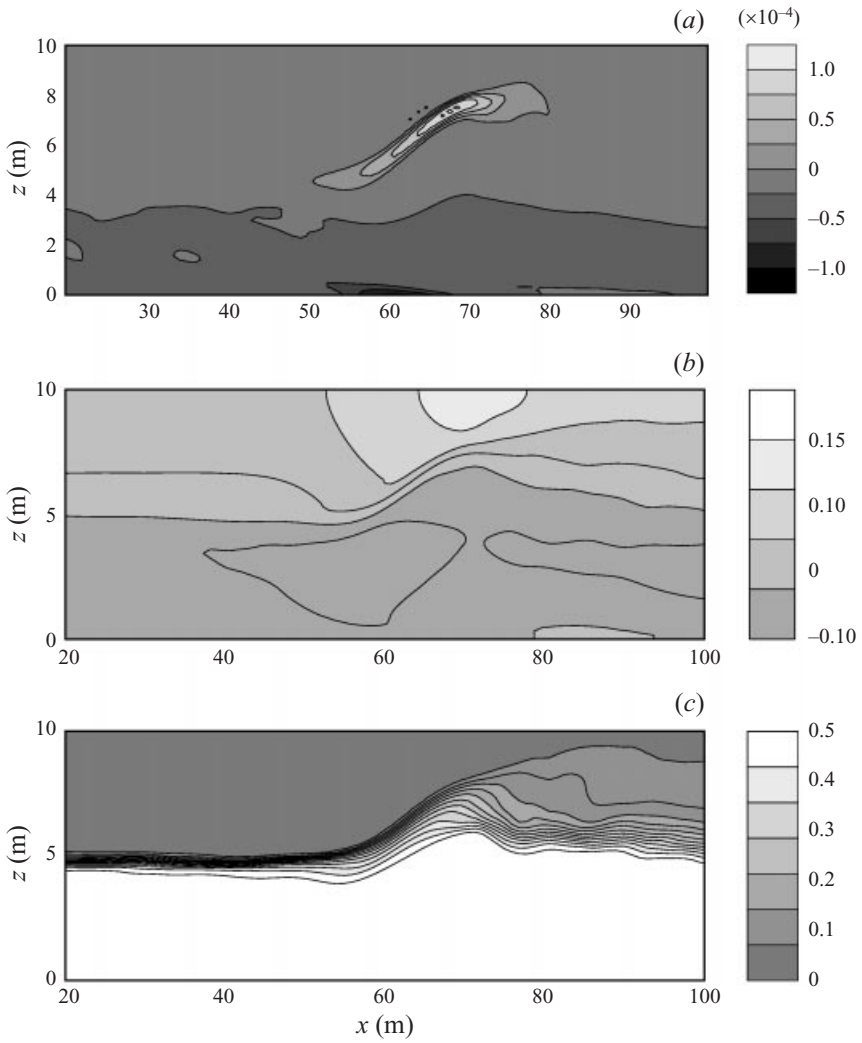

FIGURE 9. Contours of (*a*) $K_m \partial U/\partial z$, (*b*) u and (*c*) ρ for $q_r = 1.73$ with a no-slip bottom boundary condition. The inclusion of bottom friction shifts the solution to a submaximal exchange flow, in which only the upper layer is active. Mixing and stress are strong downstream of the contaction and at the bottom.

5. Submaximal exchange flow

5.1. *Overview*

We next consider the effect of bottom friction on the steady solution by changing the bottom boundary condition from free- to no-slip. Early in the temporal development there are obvious differences in the character of the flow. Instabilities associated with the propagating bores are more frequent and more intense than for the runs in §4. In steady state the flow strongly resembles the submaximal exchange flows of Armi & Farmer (1986). For the case shown, with $q_r > 1$, the interface is nearly flat and at mid-depth to the left of the contraction, and displaced upward to the right (figure 9*c*). Where the upper layer is thinnest, the interface is extremely active with near continual formation of billows that grow as they are advected downstream.

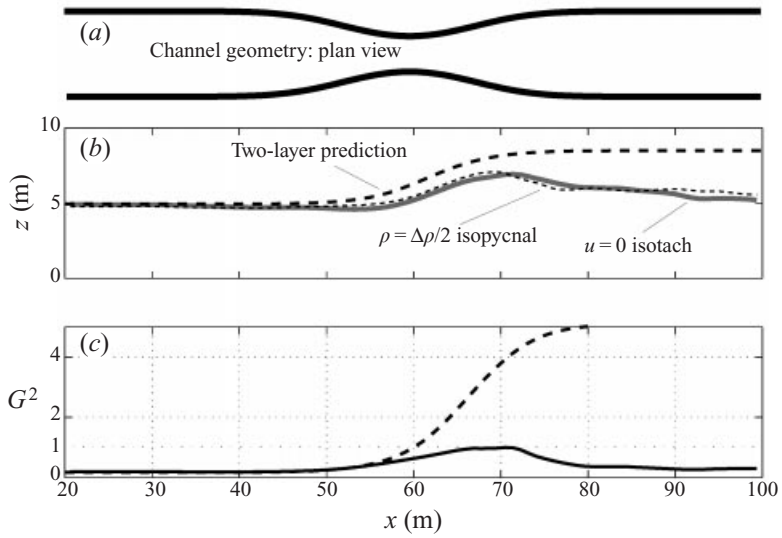

FIGURE 10. (*a*) Channel geometry, (*b*) interface heights and (*c*) composite Froude number distributions for $q_r = 1.73$ with a no-slip bottom boundary condition. The predicted curves in (*b*) and (*c*) are for a submaximal exchange flow.

Velocities in the lower layer are approximately uniform along the channel, whereas velocities in the upper layer peak downstream of the contraction. The shear stress, estimated as $K_m(\partial U/\partial z)$ and shown in figure 9(*a*), reveals the presence of enhanced stress in the bottom boundary layer, though the bed stress is less than the peak interfacial stress associated with the billows downstream of the contraction.

5.2. *Two-layer decomposition*

Because of the obvious change in flow regime, we compare this simulation with hydraulic predictions for submaximal exchange flow. A submaximal flow is characterized by a single control point (at the throat), and we therefore require additional information to solve the system of equations describing the inviscid solution. Armi & Farmer (1986) suggest specifying the net transport and the reservoir condition (i.e. the height of the interface in the reservoir where velocities have fallen to zero). This is impractical for our situation where we have modelled a limited domain. Rather, we determine the internal energy of the system ($\Delta H = (u_1^2 - u_2^2) - y_1$) at the exit region. This, together with the net transport, permits a prediction of the submaximal flow.

The predicted interface (figure 10) is flat to the left of the contraction, rising such that $G^2 = 1$ in the throat. The upper layer thins and supercritical flow is predicted to the right of the contraction. This is a reasonable qualitative representation of the simulated flow. The prediction corresponds well with the simulated interface height and G^2 to the left of the contraction, but in contrast with the predictions, critical conditions occur only briefly and well downstream of the throat. Unlike the flows with a free-slip bottom, the velocity and density interfaces overlay each other throughout the domain, both exhibiting obvious transitions near $x = 70$ m.

The idealized submaximal exchange prediction is matched to the model results based on the net transport Q rather than the ratio q_r. This is done because when q_r is used to match solutions, the predicted layer transports differ by as much as 50%, whereas when net transport is matched, the layer transports differ by 15–30%, as in

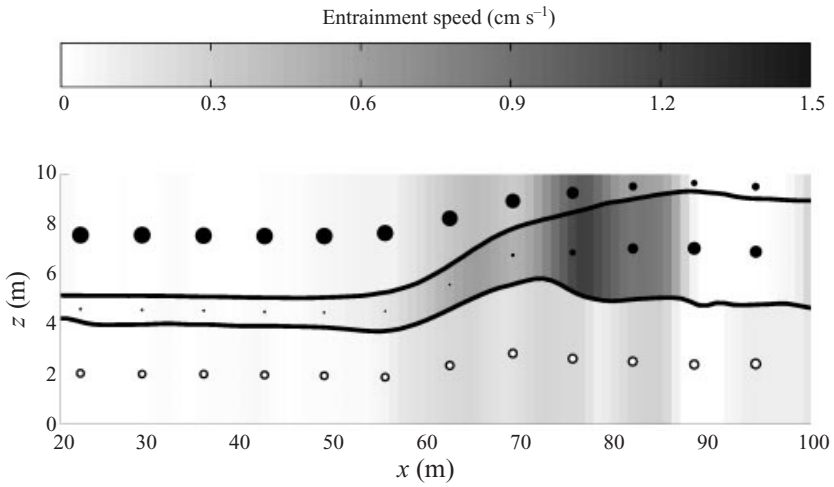

FIGURE 11. Graphic presentation of the flow rates and entrainment rates for the no-slip run where $q_r = 1.73$, as in figure 7.

the previous comparisons. This leads to a somewhat different predicted q_r (1.94) than the simulated $q_r = 1.73$. The pressure drop needed to drive a net transport in the simulation is only 40% of the predicted pressure drop. This is the smallest pressure drop used in any of the reported calculations.

5.3. *Three-layer decomposition*

Viewing the simulation as a three-layer flow highlights the dramatic change in the role of the interfacial layer in a submaximal exchange flow (figure 11). To the left of the contraction the interfacial layer is of constant thickness and essentially stagnant. Entrainment into the layer is minimal. To the right of the contraction, the interfacial layer becomes quite thick, occupying $\approx$ 40% of the depth of the fluid, and carries more of the transport than the upper-layer at the channel exit. Maximum entrainment occurs downstream of the contraction, and upper-layer fluid is preferentially entrained. The lower-layer transport is essentially uniform except for moderate detrainment from the layer upstream of the throat. Bottom friction breaks the symmetry in flow properties across the contraction.

The bias towards strong mixing only downstream of the contraction is also apparent in the distribution of eddy viscosity (figure 12). Peak values of K_m are only half the magnitude seen in the free-slip simulations (cf figure 8). A broad region of the flow around the interface exhibits elevated eddy viscosity, which together with the bottom boundary layer, produces almost the same average eddy viscosity as the free-slip simulations. The region of greatest K_m gradually moves above the main pycnocline downstream of the contraction, in contrast to the free-slip runs in which large K_m was strictly confined to the pycnocline. Eddy viscosity in the bottom boundary layer is minimal upstream of the contraction, reaches a maximum in the throat, and remains elevated downstream of the contraction, where the flow would be supercritical in a maximal exchange flow.

The broad expanse of elevated K_m downstream of the contraction is the result of strongly time-dependent flow. Snapshots of the instantaneous velocity and density fields at 250 s intervals (figure 13) illustrate the nature of the time-dependence. In stark contrast to the maximal exchange flows, which were generally stable at resolved

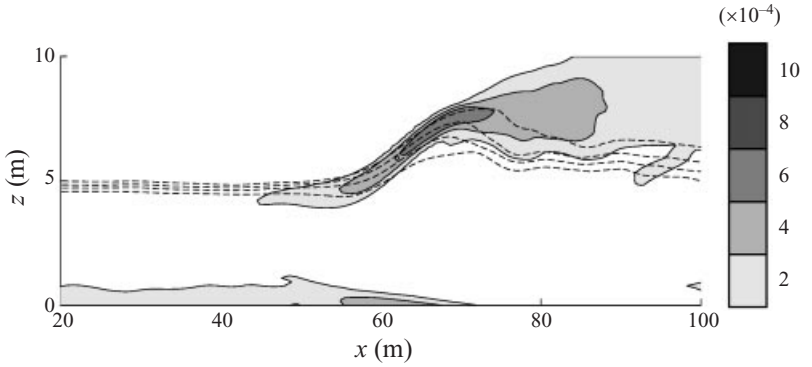

FIGURE 12. Contours of K_m for the no-slip run where $q_r = 1.73$, overlain with isopycnals between 0.1 and 0.4 kg m^{-3}. Note the asymmetry of the distribution of K_m about the contraction, in contrast to the free-slip model runs.

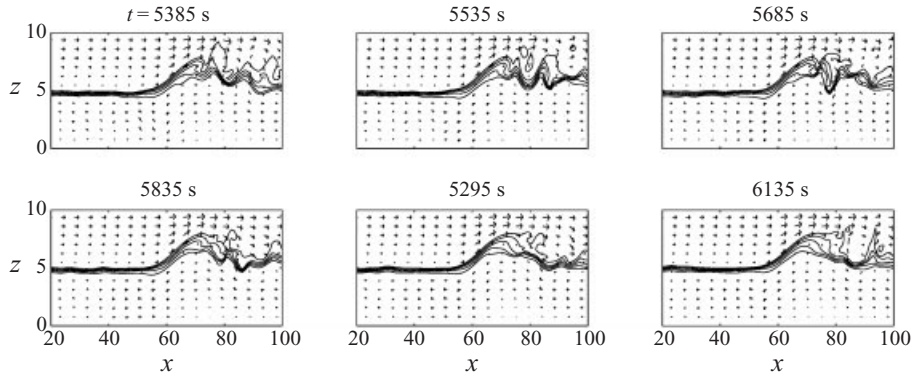

FIGURE 13. A series of snapshots of the velocity vectors overlain with density contours at 250 s intervals to demonstrate the time-dependence of the flow when bottom friction is included.

scales, the submaximal flow is highly intermittent downstream of the contraction. Shear instabilities are regularly shed from the region where the flow achieves $G^2 = 1$ (near $x = 70$ m) that are advected out of the right-hand side of the domain. Averaging these features over time produces a smooth but broad region of enhanced viscosity to the right of the contraction. To the left of the contraction the pycnocline is sharp, the flow is stable, and except for occasional small-amplitude waves, shows little time-dependence.

The inclusion of bottom friction results in qualitative changes in the solution. Though the stress associated with the bottom boundary is not a dominant feature, and does not increase the average eddy viscosity in the domain, maximal exchange solutions are no longer observed. The model solutions are a form of submaximal exchange but require considerably weaker external forcing than predicted by inviscid theory. Simulated layer transports exceed predictions by 15–30%, similar to the discrepancy observed in comparing the free-slip simulations with maximal exchange predictions. The interfacial layer plays an important role only on the downstream side of the contraction, where it reaches a thickness close to half the fluid depth and carries the majority of the downstream transport. Upstream of the contraction the interfacial layer is thin and essentially stagnant. The other hallmark of the no-slip

runs is that they are highly time-dependent, exhibiting a continuous shedding of shear instabilities downstream of the hydraulic control.

6. Discussion

Our intent in this study is to examine how the inclusion of mixing and dissipation modifies the solution of an exchange flow relative to the predictions of inviscid, hydrostatic theory. This has been accomplished by posing an initial value problem that can be solved numerically and has an exchange flow as its steady-state solution. The numerical technique permits us to study the flow of a continuously stratified fluid in an open channel in detail, subjecting the simulated flow to analyses that would not be feasible in laboratory or field experiments. This approach, however, is currently limited to idealized channels (Winters *et al.* 2000) and suffers from lack of quantitative confidence in the parameterization of subgrid-scale turbulence. Nevertheless, simulations such as those presented here allow the important dynamics of inter-layer exchange to be explored systematically and provide a context in which simplified models parameterizing these processes might be tested.

Though quantitative comparisons between idealized two-layer hydraulic theory and the numerical simulations have been made, care should be used in interpreting and generalizing the results. First, there is no absolutely justifiable scheme for decomposing a continuously varying flow into two layers as the theory demands. Though we have chosen to use a velocity-based decomposition, other choices might also be made. Further, the theory is fundamentally based on the concept of conservation of transport within layers, a condition which is violated to first order in the simulations. Given this, it is not at all clear how to select the 'equivalent' idealized problem to compare with. We have chosen the idealized problem with q_r matching the simulations, though again, other choices might also be reasonable. Finally, the simulations discussed represent only a limited range of the relevant parameter space. The depth to width aspect ratio and the abruptness of the contraction will clearly influence the flow but have been held fixed in this study.

6.1. *Comparison to two-layer theory*

Analysing the modelled results as a two-layer flow, recognizing the uncertainties inherent in such a decomposition, facilitates comparison with two-layer inviscid theory. Comparison of the model results with the predictions on a Froude number plane (e.g. Armi & Farmer 1986) demonstrates that the addition of interfacial friction does not fundamentally change the maximal exchange solutions (figure 14*a–c*). Two supercritical regions bound the central subcritical region, satisfying the defining requirement of a maximal exchange flow (Armi & Farmer 1987). Quantitatively, however, much more of the flow is subcritical than predicted. For example, when $q_r \approx 1$ inviscid theory predicts that the two control points collapse to a single point and that the flow is essentially supercritical everywhere. The simulations show no such coalescence of the controls and that, in general, the Froude numbers are systematically smaller than predicted. As predicted by Pratt (1986), friction acts to shift the site of the throat control downstream, but it also shifts the virtual control upstream. The regions of supercritical flow are largest on the downstream side of the contraction, but the flow reverts to a subcritical state before leaving the domain in most cases.

The relatively low simulated Froude numbers are the combined result of thicker than predicted active layers and slower than predicted layer velocities. As indicated in table 1, these conditions lead to enhanced layer transports relative to hydraulic

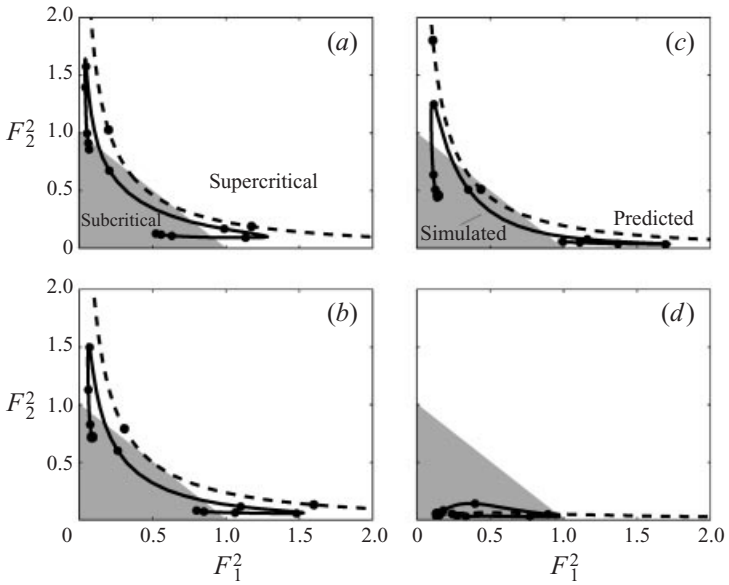

FIGURE 14. Simulated (solid) and predicted (dashed) solution curves plotted on a Froude number plane for (*a*) $q_r = 0.59$, (*b*) $q_r = 1.02$, (*c*) $q_r = 1.92$ and (*d*) $q_r = 1.73$. In the shaded region of the Froude number plane the flow is subcritical. Dots along the curves mark approximately 6 m intervals along the channel. Plots (*a–c*) are maximal exchange solutions and plot (*d*) is a submaximal exchange solution.

predictions. Increased transport thus results not from accelerated flow speeds but from a shift in the locations of hydraulic control together with an increase in layer thickness at the new control points. This appears to be the dominant effect of interfacial friction in the maximal exchange simulations.

The addition of bottom friction (figure 14*d*) qualitatively changes the solution, moving the flow into a submaximal regime. The flow is subcritical everywhere except the site of billow generation, and at which point the flow barely reaches $G^2 = 1$. From a practical point of view, it would be almost impossible to define such a flow as hydraulically controlled with field observations because of the lack of any significant region of supercritical flow. As in the cases with interfacial friction alone, the position of the control is shifted, resulting in a larger layer thickness at the control and correspondingly enhanced transport.

The issue of how this submaximal flow was forced is subtle. We do not specify the interface positions at either end of the channel, only the density of the inflows and the magnitude of the barotropic pressure drop. Lock exchange initial conditions, in this case over a no-slip bottom boundary, evolve toward a steady submaximal exchange. This state does not arise from flooding of a virtual control through externally imposed end conditions. Rather, supercritical flow is inhibited on one side of the contraction because bed friction limits the lower-layer velocity. This additional mechanism retarding the flow fundamentally alters the force balance in the lower layer in such a way that a large change in layer thickness is no longer required. Consequently, the change in upper-layer thickness through the contraction is correspondingly reduced.

With a no-slip bottom boundary, an exchange flow with q_r near 2 requires a significantly smaller pressure drop across the channel than for the case with interfacial

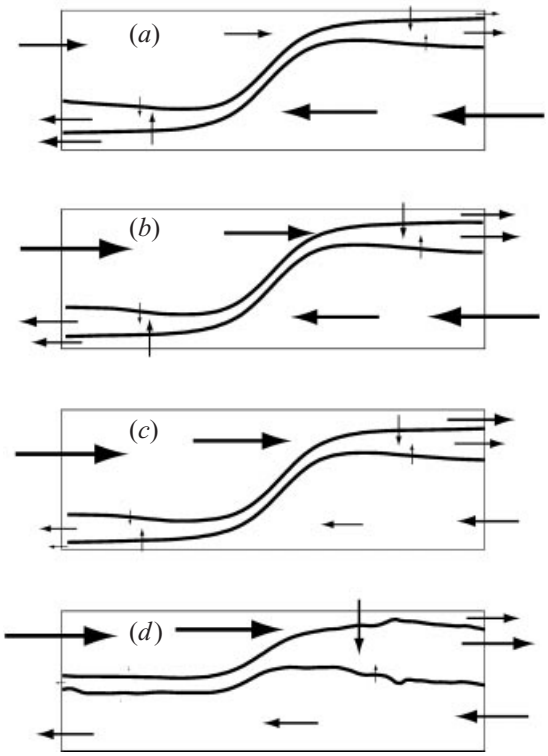

FIGURE 15. Schematic representation of the horizontal and vertical transports in a three-layer system for (*a*) $q_r = 0.59$, (*b*) $q_r = 1.02$, (*c*) $q_r = 1.92$ and (*d*) $q_r = 1.73$. Arrows show the magnitude and direction of the transports. Magnitudes have been normalized by the maximum transport in each panel.

friction alone. When the no-slip case was run with the same pressure drop as the free-slip case, the combination of the barotropic pressure gradient and bed friction nearly arrested the flow in the lower layer. The upper-layer transport thus greatly exceeded that in the lower layer and the resulting q_r was slightly greater than 15. When a much reduced pressure drop is imposed, bed friction balances the acceleration of the lower layer by the baroclinic pressure gradient, and interfacial friction is the principal force balancing the barotropic forcing of the upper layer. Apparently, the pressure gradients needed to sustain an exchange flow in the presence of friction are considerably less than in its abscence.

6.2. *Three-layer analysis*

Although two-layer inviscid theory gives reasonable predictions of the layer transports, even when frictional effects are included (and assuming one knows when to use a submaximal exchange solution), it provides no guidance on rates of entrainment and mixing between the layers. Bray *et al.* (1995) in their analysis of observations from the Strait of Gibraltar emphasize the importance of the interface in carrying horizontal transport, noting that its existence implies strong vertical exchange between layers. We have adopted their description of the flow as a simple means of quantifying the role of the interfacial layer in the simulation results.

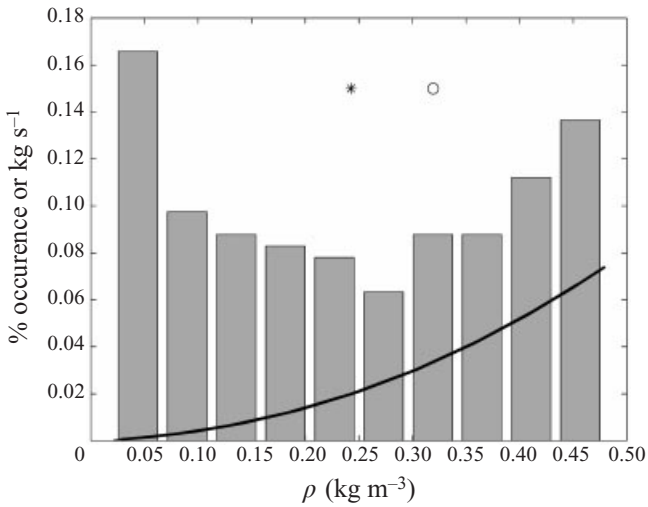

FIGURE 16. Histogram of density (bars) and density flux (solid line) within the interfacial layer between 20 and 40 m showing the preferential transport of dense water in this case (maximal exchange, $q_r = 0.59$). Note than the average density (*) is considerably less than the flux-weighted average (○).

The three-layer analysis presented earlier can be represented schematically as transports in and between layers at the ends and middle of the channel (figure 15). In each plot the transport values have been normalized by the maximum layer transport. A number of features are common to all cases and are discussed below.

Entrainment into the interfacial layer is preferentially from the faster of the bounding layers. In the vicinity of the hydraulic controls, this is the thinner of the two layers. The rates of entrainment are large, being as high as 30% of the transport of the faster layer, and as much as 20% of the slower moving layer. In the case of submaximal exchange the values are even more extreme, with as much as half of the transport carried by the upper layer being entrained into the interfacial layer. This analysis gives a rather different picture of entrainment than the two-layer view (see Δq_1 in table 1) in which the faster moving layer entrains fluid from the slower moving layer at a slower rate.

A subtle point is that the average density of the interface is not necessarily the flux-weighted average of the inflow densities. If the interface were a well-mixed layer, its density would reflect the preferential entrainment of fluid from the faster moving bounding layer, e.g. the average interface density would exceed 0.25 kg m^{-3} to the left of the contraction. However, the interface is not well mixed, and the various density classes in it are advected at different rates (figure 16). In the simulations, the average interface density is always near $\Delta\rho/2$ whereas the flux-weighted average is often 20% smaller (to the right of the contraction) or larger (to the left of the contraction). Care should be exercised when interpreting density measurements alone.

The net transport in the interfacial layer is always away from the throat of the contraction. Although the flow within the layer may be bidirectional in places, the mean transport is in the same direction as the thinner, faster moving layer. The fraction of the transport carried by the interface is typically large, being equal to or greater than the transport carried by the bounding layer that is moving in the same direction. This indicates that more than half of the fluid moving away from the contraction has undergone mixing with the opposing stream or, to a lesser extent, is

recirculating fluid from the slower moving layer. Note the similarity between figure 15 here and figure 21 in Bray *et al.* (1995). The submaximal exchange case is different. Here there is very little transport to the left of the contraction. The absence of a virtual control results in a stable flow upstream of the contraction with relatively low eddy diffusivity (figure 12). Little fluid is entrained from the bounding layers.

The existence of a net (cross-sectional averaged) flow, i.e. $q_r \neq 1$, leads to maximum entrainment on the downstream side of the contraction (to the left when $q_r < 1$ and to the right when $q_r > 1$). The fraction of fluid lost from the bounding layer carrying the most transport is less, however, than for the $q_r \approx 1$ case. The interface carries less than half the transport downstream of the contraction, but as much as 2/3 of the transport on the upstream side for the maximal exchange cases.

The interlayer transports can be interpreted in terms of mixing and recirculation. For example, consider a passive tracer C entering the lower layer in figure 15(a). Before passing through the contraction 15% of the flux of C would be lost to the interfacial layer and recirculate out the right-hand end of the channel. Of the 85% passing through the contraction, about 30% would be diluted by mixing with overlying fluid, and the remaining 55% would leave the left-hand end of the domain unaltered. In our simulations, these numbers are fairly typical, in that roughly half the fluid in a bounding layer that at some point is supercritical is lost to the interfacial layer.

Though the simulated volumetric transports are increased relative to two-layer predictions, presumably owing to a shift in the locations and conditions of hydraulic control, net horizontal tracer transports are reduced by 10–15% for the simulated maximal exchange flows as a result of dilution through mixing. This finding is consistent with the laboratory measurements of Helfrich (1995) who observed a reduction in salt transport of approximately 15%, attributing it to the formation of a stratified, sheared interfacial layer through mixing. These results suggest that mixing in the vicinity of hydraulic controls is a process of considerable importance in determining the overall circulation and exchange between basins connected by straits or channels.

Though much of the theoretical work focuses on maximal exchange, submaximal exchange flows may be equally relevent. The submaximal case simulated appears to be a reasonable qualitative representation of the observed flow near the central contraction in the Bosphorus Strait (see e.g. Oğuz *et al.* 1990). To the north of the contraction, where the interface is approximately at mid-depth, the observed flow is stable and subcritical. To the south of the contraction the interface is much shallower, the upper layer flow is accelerated and turbulence is greatly enhanced. These are the essential features of the flow shown in the figure 13. The simulations suggest that submaximal flow can result from local conditions, in this example through bottom stress, and may not require the existence of hydraulic controls far up- or down-stream. We do not mean to suggest that bottom friction necessarily induces a shift to submaximal exchange but do note that as the bottom boundary layer thickens to an appreciable fraction of the lower layer thickness, this becomes more likely.

This work was supported by the Office of Naval Research (Code 322, Physical Oceanography) under grants N00014-92-J-1180 and N00014-96-1-0616. We appreciate the many discussions with Mike Gregg, D'Asaro, Frank Henyey, Greg Ivey and Tim Finnigan. Computational resources were provided by the Multi-Discipline Group at the University of Washington Applied Physics Laboratory and the Skidaway Institute of Oceanography.

Appendix A

A.1. *Subgrid-scale closure*

Unless the flow is to be resolved to the dissipative scales, i.e. to approximately millimetre scales, turbulent transport of mass and momentum must be parameterized in terms of the resolved-scale flow. The parameterization employed here, following the Smagorinsky (1963) approach, is based on an assumed steady local balance for turbulent kinetic energy

$$\varepsilon = S^2 - \frac{g}{\rho_0}\overline{\rho w} \tag{A 1}$$

where ε is the dissipation rate of turbulent kinetic energy and $S^2 = \overline{u_i u_j}\partial_j U_i$ is the rate of shear production. Lower-case variables represent subgrid-scale quantities, upper case the resolved-scale quantities and the overbar indicates spatial and/or temporal averaging over the subgrid scales.

Assuming that the turbulent correlations can be written in flux-gradient form, i.e. that

$$\overline{u_i u_j} = -K_m\left(\frac{\partial U_i}{\partial x_j} + \frac{\partial U_j}{\partial x_i}\right), \tag{A 2}$$

$$\overline{\rho w} = -K_T\frac{\partial \Lambda}{\partial z}, \tag{A 3}$$

the dissipation rate ε can be written in terms of the resolved-scale quantities as follows:

$$\varepsilon = K_m\left(S'^2 - N'^2\right), \tag{A 4}$$

where

$$S'^2 = \frac{1}{2}\left(\frac{\partial U_i}{\partial x_j} + \frac{\partial U_j}{\partial x_i}\right)^2 \quad \text{and} \quad N'^2 = -\left(\frac{K_T}{K_m}\right)\left(\frac{g}{\rho_0}\right)\frac{\partial \Lambda}{\partial z}.$$

Here Λ indicates the total resolved scale density.

Following Smagorinsky (1963), and based solely on a dimensional argument, we write

$$K_m = (C_s\Delta)^{4/3}\varepsilon^{1/3} \tag{A 5}$$

where Δ is a length scale, taken in practice as the nominal grid spacing $(\mathrm{d}x\ \mathrm{d}y\ \mathrm{d}z)^{1/3}$, and C_s is the dimensionless Smagorinsky constant. Solving for ε and substituting into (A 4) yields an expression for the eddy viscosity K_m in terms of local values of the resolved-scale flow

$$K_m = (C_s\Delta)^2\sqrt{S'^2 - N'^2}. \tag{A 6}$$

Provided that $S'^2 - N'^2 > 0$, this expression is used for both K_m and K_T in the governing equations. If $S'^2 - N'^2 < 0$, which occurs in regions of weak shears with strong stable stratification, K_m is held fixed at $10^{-6}\,\mathrm{m^2\,s^{-1}}$. For the simulations reported here, the Smagorinsky constant C_s was taken to be 0.17. This choice is in accord with previously used values. For example Siegel & Domaradzki (1994) obtained good agreement with predicted energy spectra for decaying stratified turbulence using a value of 0.15. Kaltenbach, Gerz & Schumann (1994) used $C_s = 0.17$, in studies of spatially homogeneous turbulence in a stably-stratified shear flow, though in their study, buoyancy and the contribution of the mean shear to S' were neglected. A value of 0.5 was used by Skyllingstad & Denbo (1994) in simulations of internal

wave–mean shear interactions in the equatorial undercurrent. In each of the studies cited, the turbulent Pr was taken as unity, i.e. $K_T = K_m$.

Though in principle a numerical study permits quantitative consideration of mixing and dissipation in exchange flows, the simulation results should perhaps be interpreted only qualitatively unless or until approximation errors associated with the closure scheme can be established. Though different choices of closure could be made, and perhaps to some extent justified, there is currently no demonstrably valid scheme applicable across the range of dynamical conditions generated in these simulations. We have thus opted for the relative simplicity of the fixed-coefficient Smagorinsky scheme. Further development or assessment of alternative closure schemes is beyond the scope of this initial work.

A.2. *Boundary conditions*

Before discussing the boundary conditions, it is necessary to sketch the numerical treatment of the pressure. To do so, we rewrite equations (6)–(7) as

$$\frac{\partial}{\partial t}\boldsymbol{u} = \mathscr{F}_u - \frac{1}{\rho_0}\tilde{\nabla}p, \tag{A 7}$$

$$\frac{\partial}{\partial t}\rho' = \mathscr{F}_\rho. \tag{A 8}$$

where $\mathscr{F}_u$ and $\mathscr{F}_\rho$ are defined by the correspondence between (6)–(7) and (A 7)–(A 8).

Time integration is carried out in two stages. Assuming the velocity and density fields are known at time t, and the solutions are desired at time $t+\Delta t$, an intermediate velocity vector $\boldsymbol{u}_*$, is defined where

$$\boldsymbol{u}_*(x, y, z) = \boldsymbol{u}(x, y, z, t) + \int_t^{t+\Delta t} \mathscr{F}_u \, \mathrm{d}t. \tag{A 9}$$

Introducing the function P such that

$$\boldsymbol{u}(x, y, z, t + \Delta t) = \boldsymbol{u}_* - \frac{\Delta t}{\rho_0}\tilde{\nabla}P \tag{A 10}$$

it follows that

$$\nabla P = \frac{1}{\Delta t}\int_t^{t+\Delta t} \nabla p \, \mathrm{d}t \tag{A 11}$$

showing that the function P is related to the fluid pressure p through a time average over the time interval Δt.

At each time step, u_* is approximated from (A 9) using an explicit integration scheme to estimate the integral over a time step Δt. An elliptic equation for P is then obtained by taking the divergence of (A 10) and imposing the incompressibility condition (8) on $\boldsymbol{u}(x, y, z, t + \Delta t)$:

$$\nabla^2 P = \frac{\rho_0}{\Delta t}\nabla \cdot \boldsymbol{u}_*. \tag{A 12}$$

In practice, the equations are transformed to curvilinear coordinates prior to numerical solution and the transformed version of (A 12) is a general, second-order elliptic equation with mixed derivatives and spatially variable but time-independent coefficients. The source term, however, depends on the computed $\boldsymbol{u}_*$ and thus varies in time.

Two types of boundary conditions are required in order to fully constrain P. At

solid walls, i.e. at the bottom, at the rigid lid and at the sidewalls, the value of $\partial P/\partial n$ is determined by resolving equation (A 10) into the directions normal the walls and imposing no flow through the walls. This is conveniently implemented numerically on the orthogonal, boundary-fitting grid because velocity components locally oriented tangentially and perpendicularly to grid lines are used as primitive variables in the algorithm. These Neumann conditions on P are used for both free-slip walls where $\partial u/\partial n = 0$ and for no-slip walls where $\boldsymbol{u} = 0$.

The up- and down-stream computational boundaries do not correspond with physical boundaries. Exact boundary conditions are thus unknown and must be modelled. At these locations, the computed density field is cross-channel averaged and integrated in depth to produce time-dependent hydrostatic density profiles at each end of the domain. At each time step, P is then constrained to satisfy Dirichlet boundary conditions determined by these profiles, augmented by the specified barotropic pressure drop across the channel. When the flow is two-dimensional and truly hydrostatic, these boundary conditions can be expected to work well with minimal reflection of outgoing signals. When the outflow is characterized by non-hydrostatic wave motions, as is frequently the case here, significant reflections are to be expected. To minimize these reflections, sponge layers with significantly enhanced eddy viscosity are placed adjacent to the computational boundaries. All results presented are taken from the 'test section' interior to the regions of artificially enhanced damping. In this scheme, outgoing waves are damped as they approach the boundaries and, to the extent that reflections occur, they are further damped as they return toward the 'test section'.

By specifying P and employing one-sided discretizations near the up- and down-stream boundaries, no additional conditions are required for the velocity. The density of the inflowing fluid, however, must be specified. Adopting the convention that the dense undercurrent flows from right to left, we specify that $\rho = \rho_1$ at the left-hand edge $x = 0$ when $u > 0$ and $\rho = \rho_2$ at the right-hand edge $x = L_x$ when $u < 0$ where ρ_i are constant values with $\rho_2 - \rho_1 = \Delta\rho > 0$. We note that for these inflow conditions, only fluid at the extreme values ρ_1 and ρ_2 is advected into the computational domain from up- and down-stream; there is no external source of intermediate-density fluid.

REFERENCES

Armi, L. & Farmer, D. 1986 Maximal two-layer exchange through a contraction with barotropic net flow. *J. Fluid Mech.* **164**, 27–51.

Armi, L. & Farmer, D. M. 1987 A generalization of the concept of maximal exchange in a strait. *J. Geophys. Res.* **92**, 14679–14680.

Baines, P. G. 1995 *Topographic Effects in Stratified Flows*, 1st edn. Cambridge University Press.

Bray, N. A., Ochoa, J. & Kinder, T. H. 1995 The role of the interface in exchange through the strait of gibraltar. *J. Geophys. Res.* **100**, 10755–10776.

Helfrich, K. R. 1995 Time-dependent two-layer hydraulic exchange flows. *J. Phys. Oceanogr.* **25**, 359–373.

Kaltenbach, H.-J., Gerz, T. & Schumann, U. 1994 Large-eddy simulation of homogeneous turbulence and diffusion in stably stratified shear flow. *J. Fluid Mech.* **280**, 1–40.

Lawrence, G. A. 1990 Can mixing in exchange flows be predicted using internal hydraulics? In *The Physical Oceanography of Sea Straits* (ed. L. J. Pratt), pp. 519–536. Kluwer.

Oğuz, T., Özsoy, E., Latif, M. A., Sur, H. I. & Ümit Ünlüata 1990 Modeling of hydraulically controlled exchange flow in the bosphorus strait. *J. Phys. Oceanogr.* **20**, 945–965.

Pratt, L. J. 1986 Hydraulic control of sill flow with bottom friction. *J. Phys. Oceanogr.* **16**, 1970–1980.

Siegel, D. A. & Domaradzki, J. A. 1994 Large-eddy simulation of decaying stably stratified turbulence. *J. Phys. Oceanogr.* **24**, 2353–2386.

Skyllingstad, E. D. & Denbo, D. W. 1994 The role of internal gravity waves in the equatorial current system, *J. Phys. Oceanogr.* **24**, 2093–2110.

Smagorinsky, J. 1993 General circulation experiments with the primitive equations. *Mon. Wea. Rev.* **91**, 99–164.

Winters, K. B., Lombard, P. N., Riley, J. J. & D'Asaro, E. A. 1995 Available potential energy and mixing in stratified fluids. *J. Fluid Mech.* **289**, 115–128.

Winters, K. B., Seim, H. E. & Finnigan, T. 2000 Simulation of non-hydrostatic, density-stratified flow in irregular domains. *Intl J. Numer. Meth. Fluids* **32**.